Cancer Imaging

RESEARCH Open Access

CT-based machine learning model integrating intra- and peri-tumoral radiomics features for predicting occult lymph node metastasis in peripheral lung cancer

Xiaoyan Lu[1†], Fan Liu[1†], Jiahui E[1], Xiaoting Cai[1], Jingyi Yang[1], Xueqi Wang[1], Yuwei Zhang[1], Bingsheng Sun[2*] and Ying Liu[1*]

Abstract

Background Accurate preoperative assessment of occult lymph node metastasis (OLNM) plays a crucial role in informing therapeutic decision-making for lung cancer patients. Computed tomography (CT) is the most widely used imaging modality for preoperative work-up. The aim of this study was to develop and validate a CT-based machine learning model integrating intra-and peri-tumoral features to predict OLNM in lung cancer patients.

Methods Eligible patients with peripheral lung cancer confirmed by radical surgical excision with systematic lymphadenectomy were retrospectively recruited from January 2019 to December 2021. 1688 radiomics features were obtained from each manually segmented VOI which was composed of gross tumor volume (GTV) covering the boundary of entire tumor and three peritumoral volumes (PTV3, PTV6 and PTV9) that capture the region outside the tumor. A clinical-radiomics model incorporating radiomics signature, independent clinical factors and CT semantic features was established via multivariable logistic regression analysis and presented as a nomogram. Model performance was evaluated by discrimination, calibration, and clinical utility.

Results Overall, 591 patients were recruited in the training cohort and 253 in the validation cohort. The radiomics signature of PTV9 showed superior diagnostic performance compared to PTV3 and PTV6 models. Integrating GPTV radiomics signature (incorporating Rad-score of GTV and PTV9) with clinical risk factor of serum CEA levels and CT imaging features of lobulation sign and tumor–pleura relationship demonstrated favorable accuracy in predicting OLNM in the training cohort (AUC, 0.819; 95% CI: 0.780–0.857) and validation cohort (AUC, 0.801; 95% CI: 0.741–0.860). The predictive performance of the clinical-radiomics model demonstrated statistically significant superiority over that of the clinical model in both cohorts (all $p < 0.05$).

†Xiaoyan Lu and Fan Liu contributed equally to this work.

*Correspondence:
Bingsheng Sun
sunbingsheng@tjmuch.com
Ying Liu
tjliuying2009@163.com

Full list of author information is available at the end of the article

Conclusions The clinical-radiomics model was able to serve as a noninvasive preoperative prediction tool for personalized risk assessment of OLNM in peripheral lung cancer patients.

Keywords Lung cancer, Radiomics, Occult lymph node metastasis, Tumor, Peritumoral

Introduction

According to GLOBOCAN 2020 estimates of cancer incidence and mortality produced by the International Agency for Research on Cancer, lung cancer is the leading cause of cancer death [1]. Lymph node (LN) metastasis plays a crucial role in the TNM staging system and is considered one of the most significant prognostic factors for patients with lung cancer [2]. Based on the evidence that segmentectomy or sublobectomy could provide equivalence prognosis compared to lobectomy for patients with early-stage lung cancer without LN metastasis [3–5], these limited surgery with the benefits of reducing overall complication rate, preserving lung function and better postoperative immune-nutritional status has emerged as an alternative modality in selected patients [6, 7]. Meanwhile, in contrast to the conventional notion of "more is better" regarding LN dissecting, an elevated dissected LN count is associated with poorer immunotherapy efficacy in post-resectional recurrent NSCLC [8]. Therefore, precise assessment of LN metastasis prior to surgery is vital for clinicians to create individualized treatment plans for lung cancer patients.

Computed tomography (CT), which is the standard imaging method for preoperative assessment of lung cancer, has limited value for precise determination of LN metastasis [9, 10]. Image-based preoperative evaluation of LN status mainly depends on size criterion, usually a short axial diameter larger than 10 mm is considered as the diagnostic cutoff for LN malignancy. However, benign and metastatic lymph nodes can overlap in size. Obstructive pneumonia, atelectasis, infection and interstitial pneumonia can also cause swollen lymph nodes which lead to false positives, whereas the presence of micro-metastasis in normal sized nodes could be misdiagnosed as normal even in cases with primary lung cancer smaller than 3 cm [11, 12]. A recent study has found that even if the short axis of all lymph nodes were smaller than 10 mm and SUVmax of mediastinal lesions were lower than 2.5, LN metastasis could still occur in NSCLC patients, and the incidence rate was 37.3% [13]. Thus, accurate preoperative assessment of LN status, especially precise evaluation of those LN within normal size, referred to herein as occult lymph node metastasis (OLNM), remains a challenge for radiologists.

Radiomics, proposed by Lambin in 2012 [14], is an emerging medical image analysis method that can capture mesoscopic features of the tumor concealed within medical images, which cannot be discerned by naked eyes [15]. With the help of transforming this information into analyzable high-throughput data, radiomics has unfolded a new dimension for evaluating cancer structure and biology [16]. Previous studies have shown the feasibility of developing radiomic signatures to predict LN metastasis in NSCLC [17–26]. Although these results were encouraging, some of the histopathological parameters in the proposed prediction model were only available after surgery; in addition, there was considerable variation in the distances of peritumoral expansion documented in different studies which resulted in inconsistent conclusions and potential challenges when interpreting the findings. In this study, we hypothesized that the integration of intra- and peri-tumoral radiomics features extracted from pretreatment CT images could facilitate the identification of OLNM in patients with lung cancer. We further investigated the optimal distances for peritumoral expansion and combined these radiomics data with semantic features of the primary tumor and clinical information to optimize individualized surgical strategies, ensuring adequate yet non-excessive lymph node dissection.

Methods

Study design and patient selection

This study was conducted in accordance with the Declaration of Helsinki. The requirement for patient informed consent was waived by the institutional review board due to the retrospective study design. Medical records of pathologically confirmed lung cancer patients were consecutively retrieved from the institutional database from January 2019 to December 2021. The enrolled patients met the following inclusion criteria: (1) underwent lobectomy, segmentectomy or pneumonectomy with systematic lymph node dissection; (2) preoperative chest CT images within 2 weeks before surgery and CT-based LN status was cN0 (hilar and mediastinal lymph nodes with the short-axis diameter smaller than 10 mm on CT images were diagnosed as cN0); (3) lung lesions classified as solid or partly solid, and for the latter one ground-glass opacity (GGO) component did not exceed 50%; (4) availability of clinical and pathologic data. Patients were excluded if they had a central location tumor, underwent any preoperative treatment for lung cancer, had any current or previous malignancy other than lung cancer, had multiple lung cancers, had non-measurable lesions on CT (e.g., due to atelectasis), or had unsatisfactory image quality due to respiratory artifact during CT examination. Finally, 844 patients pathologically confirmed lung cancer with cN0 status on preoperative CT images were

included in the current study, and then randomly divided into a training cohort ($n = 591$) and a validation cohort ($n = 253$) at a 7:3 ratio (Fig. 1).

Baseline demographic data (sex, age, smoking history) and laboratory analysis of routine tumor markers of lung cancer within 1 week before surgery including neuron specific enolase (NSE), carcinoma embryonic antigen (CEA), tissue polypeptide specific antigen (TPSA), squamous cell carcinoma antigen (SCC-Ag), pro-gastrin-releasing peptide (ProGRP), and cytokeratin 19 fragment (Cyfra 21 – 1) were obtained from electrical medical records. According to the guidelines of the European Association of Thoracic Surgeons, at least six LNs were dissected for each patient [27]. Post-operative pathologic results were used as the gold standard, and patients were then classified into pathological lymph node positive (pN+) and lymph node negative (pN-) groups.

CT image acquisition and analysis

All CT scans were performed from the lung apex to the bilateral adrenal glands, using multi-detector row CT systems and the detailed parameters of scanning were described in Supplementary Text 1. Two radiologists who were blinded to clinical and pathologic information (with experience of 2 years and 3 years in chest CT imaging) evaluated the following characteristics independently: (a) tumor affiliated lobe, (b) maximum axial diameter and perpendicular short axial diameter, (c) spiculation, (d) lobulation, (e) air bronchogram, (f) vacuole sign, (g) vascular convergence, (h) tumor–pleura relationship. Tumor–pleura relationship was classified into two types [28] (Fig. 2). All the other categorical variables including spiculation, lobulation, air bronchogram, vacuole sign and vascular convergence were encoded into binary variables (absence or presence). Any discordant interpretation was resolved via consultation from a third senior radiologist (Y.L. with 19 years of experience). The average for continuous variable was calculated as the final value.

Image preprocessing and volumes of interest (VOI) segmentation

To obtain a better comparison of heterogeneous imaging data using different CT devices, a linear interpolation algorithm was applied to resample the imaging data to a standardized pixel dimension size of $1.0 \times 1.0 \times 1.0$ mm^3, and then the voxel intensities were discretized using a fixed group spacing of 25Hu, a parameter commonly adopted in the literature [29, 30], in order to reduce the image noise and standardize the grayscale to achieve a stable strong resolution. Finally, normalization was performed to minimize variations in signal intensity across different imaging systems.

Tumor segmentation was manually performed by a trained radiologist (reader A) using open-source software

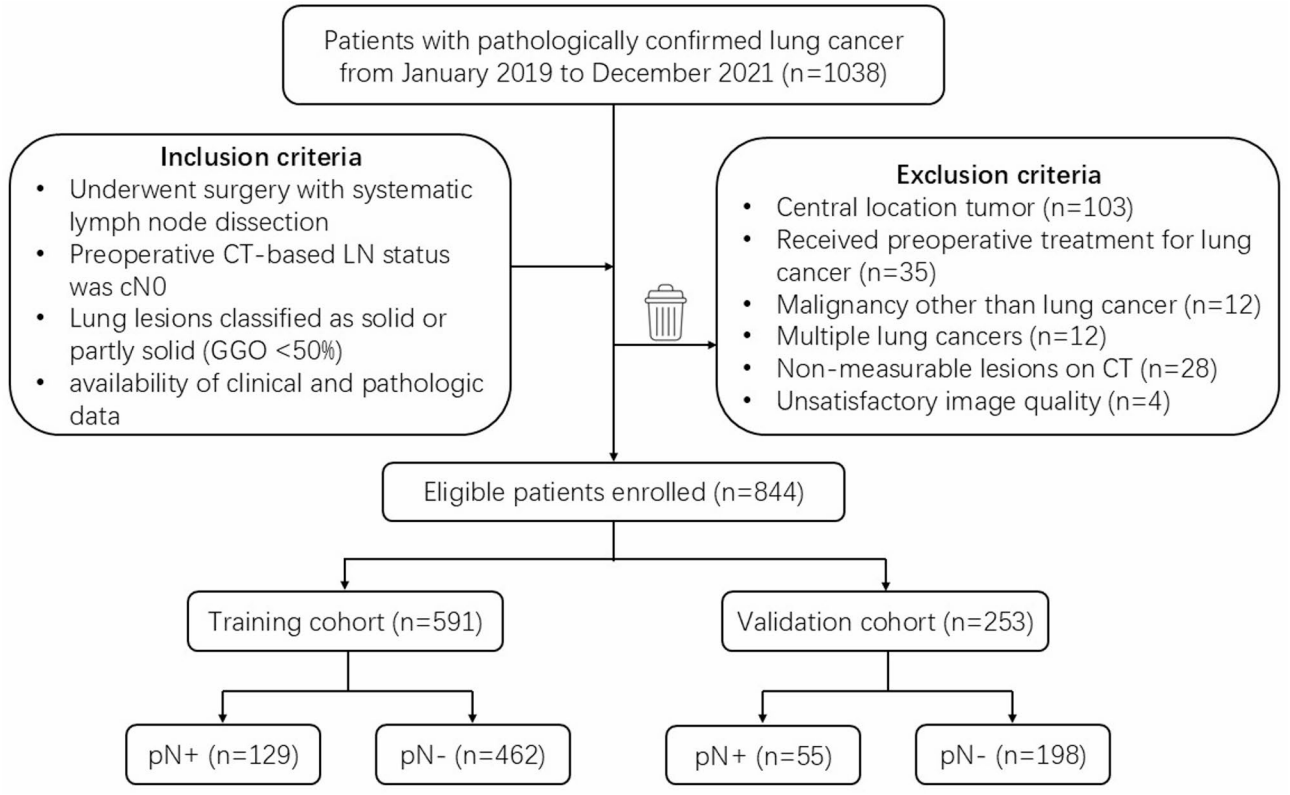

Fig. 1 Flowchart of patient selection in this study

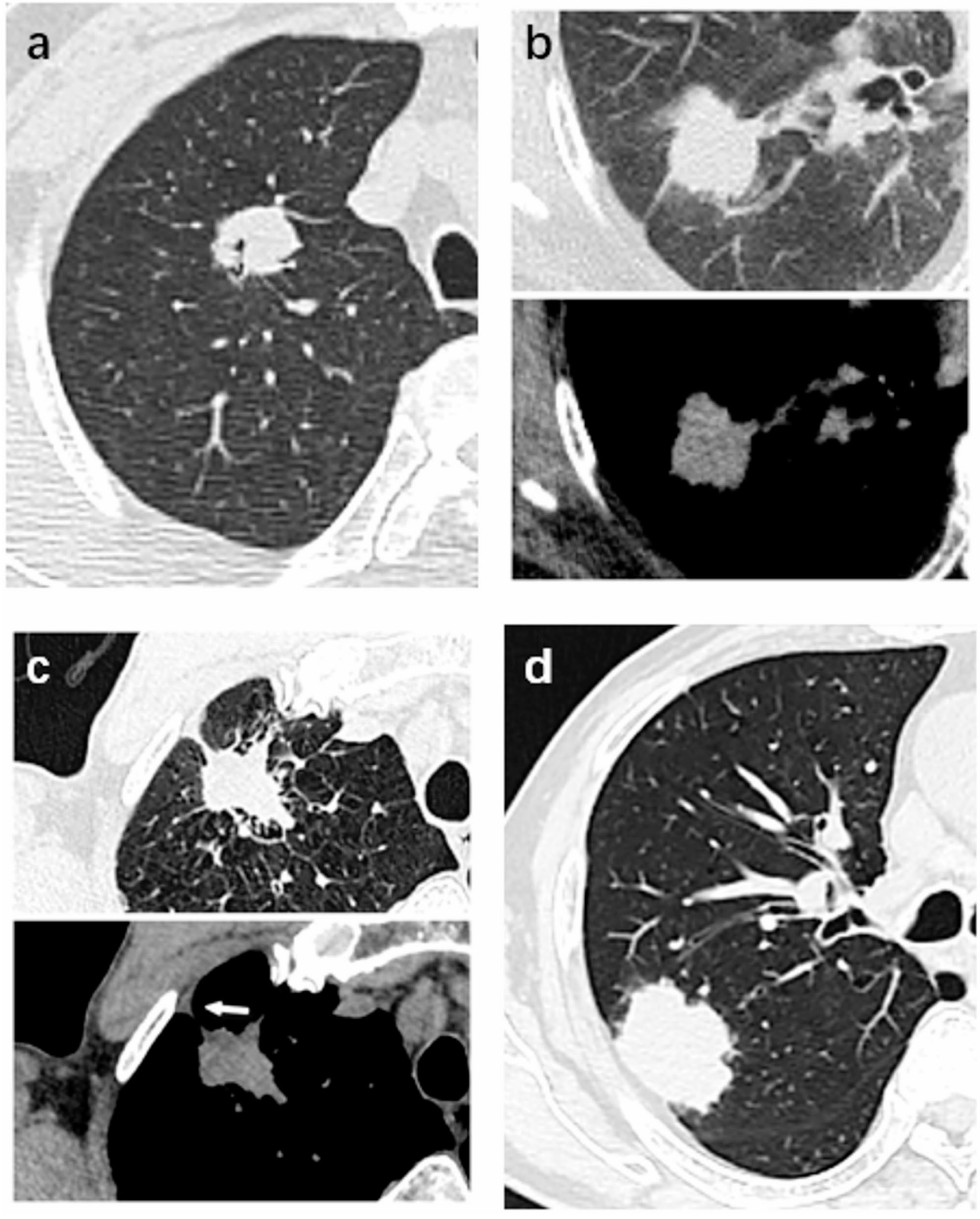

Fig. 2 Example of Type I and Type II tumor–pleura relationship. Type I, tumor was unrelated to the pleura (**a**) or manifested linear shadows between tumor and pleura on lung window images but was not observed on mediastinal window images (**b**); Type II, tumor had linear or striated pleural tags between tumor and pleura observed in both lung windows and mediastinal window images (**c**) or was attached to the pleura with a broad base (**d**)

3D Slicer (version 5.0.3). The lesion contours were delineated slice by slice on axial images in the lung window to ensure accurate boundary definition. Gross tumor volume (GTV) was contoured along the boundary of the tumor. Subsequently, GTV was dilated outward by 3 mm, 6 mm, and 9 mm along its boundary in all directions using an isotropic expansion method to ensure uniform growth. This process generated three concentric peritumoral volumes (PTV), referred to as PTV3, PTV6, and PTV9 (Fig. 3). Manual repair was performed if the outer expansion came into contact with the chest wall, diaphragm, main trachea, great blood vessels, or heart.

To ensure the stability and reproducibility of radiomics features, a subset of 40 cases was randomly chosen from the study cohort. Tumor segmentation was carried out using the same methodology by another radiologist (reader B). After a 3-month washout period, reader A performed tumor segmentation once again for these 40 patients.

Feature selection and radiomics signature development

A total of 1688 radiomics features from each VOI were extracted using FeAture Explore (FAE) software (version 0.5.7) which is a PyRadiomics-based (version 3.0) open-source software [31], including shape-based features, first-order statistical features, gray-level co-occurrence matrix (GLCM), gray-level dependence matrix (GLDM), gray-level run length matrix (GLRLM), gray-level size zone matrix (GLSZM), and neighboring gray tone difference matrix (NGTDM). All extracted radiomic features were standardized in compliance with the Image Biomarker Standardization Initiative (IBSI) guidelines [32] with detailed information presented in Supplementary Table 1. The Z-Score normalization method was utilized

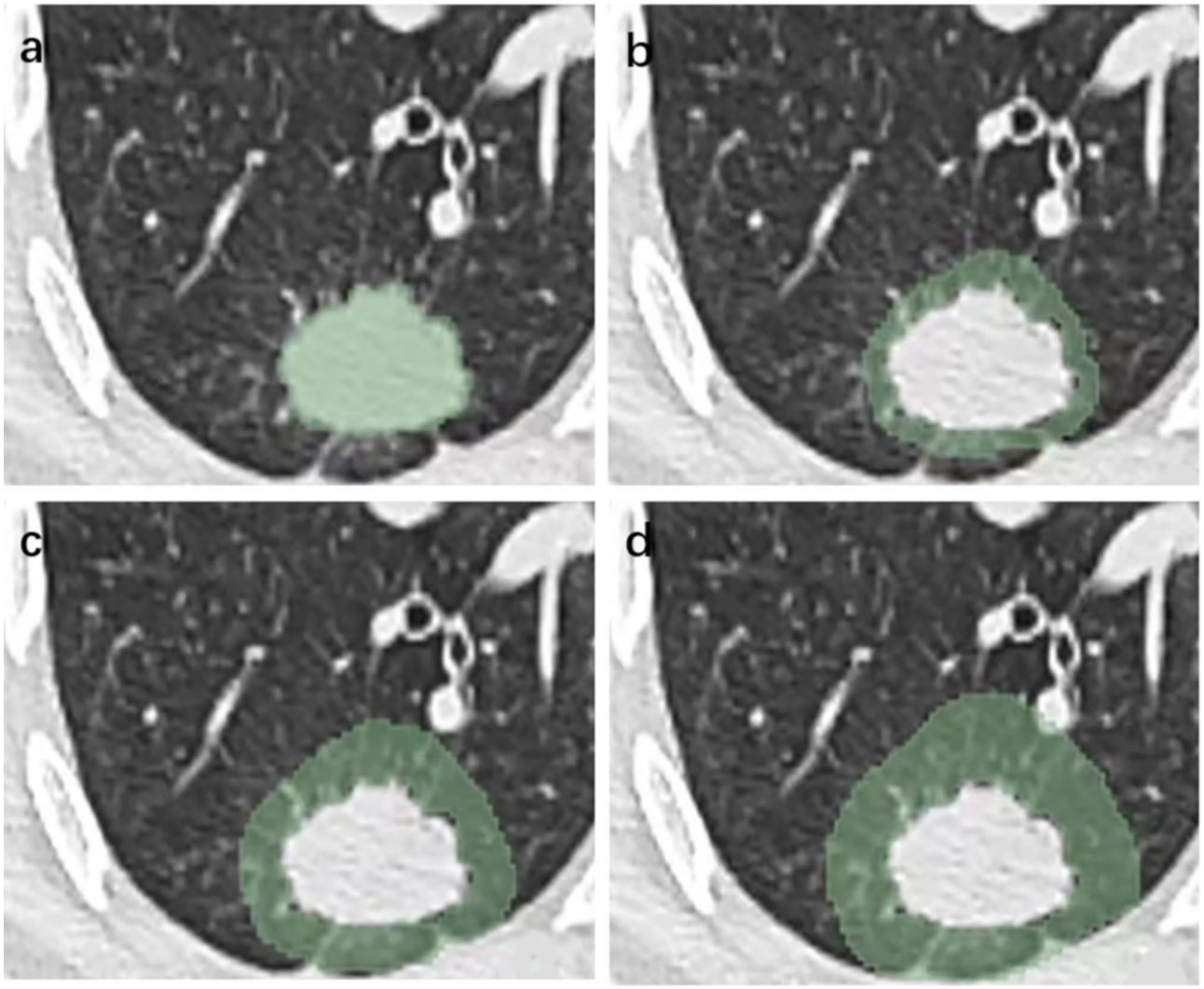

Fig. 3 Representative images of gross tumor volume (GTV) segmentation (**a**) and peritumoral volume (PTV) expansion by 3 mm (**b**), 6 mm (**c**), and 9 mm (**d**) in three dimensions

to achieve standardized processing of the radiomics feature data. Due to a substantial difference in sample size between pN + and pN- groups in this study, the synthetic minority oversampling technique (SMOTE) was employed to address data imbalance.

The inter-observer and intra-observer agreement of radiomics features was assessed using the Intraclass Correlation Coefficient (ICC), and features that exhibited an ICC value of 0.90 or higher were considered eligible and included in the subsequent analysis. We performed an independent two-sample t-test on all standardized features, retaining radiomics features with statistical significance. And then, to mitigate the adverse effects of multicollinearity, from each pair of features with Pearson Correlation Coefficient (PCC) exceeded 0.90, one of the features was randomly removed to reduce spatial dimensionality. Following that, feature selection was conducted using the minimum redundancy maximum relevance (mRMR) algorithm. Subsequently, the least absolute shrinkage and selection operator (LASSO) was applied on the training cohort to further reduce dimensionality and identify the most predictive features. The selected features were then used to construct logistic regression (LR) models, followed by 10-fold cross-validation for model evaluation. Model performance was assessed on the validation cohort, and the radiomics signature (Rad-score) achieving the highest AUC was ultimately selected as the final model. SHapley Addictive exPlanations (SHAP) analysis was employed to assess feature importance and enhance model interpretability.

Clinical model and clinical-radiomics nomogram construction

Univariable analysis was used to compare the demographic data and radiological features between pN + and pN- groups. Those factors with $p < 0.05$ in the univariable analysis were entered into the multivariable logistic regression analysis to develop clinical model in the training cohort. The clinical-radiomics nomogram, which combined optimal Rad-score and independent clinical-radiological factors was constructed using multivariable logistic regression analysis. Calibration curve was used to analyze the calibration of the clinical-radiomics nomogram. Hosmer-Lemeshow were performed to assess the goodness of fit of the models. Decision curve analysis (DCA) was conducted to determine the clinical utility of the optimal predictive model.

Statistical analysis

The statistical analysis was performed using R (version 4.2.1) and SPSS 25.0. Continuous variables were expressed as mean ± standard deviation (SD) or median (interquartile range) and compared by using Student t-test or the Mann–Whitney U test. Categorical variables were expressed as a number (percentage) and compared by chi-square test or Fisher exact test. Univariable and multivariable analyses were performed using binary logistic regression analysis to explore potential risk factors for OLNM. Receiver operating characteristics (ROC) curve for each model was plotted, with the cutoff chosen to maximize the Youden index, and the corresponding accuracy, sensitivity, and specificity were calculated to evaluate the predictive performance. Delong test was used to compare the differences in AUC values among different models. A two-sided $p < 0.05$ considered statistical significance.

Results

Clinical and CT imaging characteristics

In the whole cohort, 184 of pN + patients were under staged as cN0 according to CT evaluation, with a false negative rate of 21.8% (184/844). The baseline demographic data and laboratory analysis of routine tumor markers are presented in Table 1. There were no significant differences regarding demographic data between training and validation cohorts (all $p > 0.05$). Rate of LN metastasis was 21.8% (129 of 591) and 21.7% (55 of 253) in the training and validation cohorts, respectively, without significant difference ($p = 0.977$). Patients with CEA level higher than upper limits were more likely to have LN metastasis in both training and validation cohorts ($p < 0.001$; $p = 0.020$), while there were no statistically significant differences with regard to other serum tumor markers, age, sex, smoking history, or histologic type between pN + and pN- groups (all $p > 0.05$).

CT characteristics of the primary tumor are shown in Table 2. Tumors with OLNM tended to have larger tumor size than those without LN metastasis (all $p < 0.001$). The presence of lobulation sign and tumor with type II tumor–pleura relationship were more frequently observed in pN + group compared with pN- group in both training and validation cohorts (all $p < 0.001$). The integrated clinical model identified CEA level (odds ratio [OR], 2.408; 95% confidence interval [CI]: 1.564–3.706; $p < 0.001$), lobulation sign (OR, 2.627 95% CI: 1.376–5.013; $p < 0.001$) and tumor–pleura relationship (OR, 2.476; 95% CI: 1.543–3.972; $p < 0.001$) as independent predictors for OLNM (Supplementary Table 2). The ROC analysis yielded AUCs of 0.676 (95% CI: 0.628–0.724) in the training cohort and 0.706 (95% CI: 0.637–0.775) in the validation cohort, indicating that the model had moderate discriminative ability in distinguishing peripheral lung cancer patients with and those without OLNM.

Radiomics feature selection and signature construction

Those radiomics features with low reproducibility which had intra- or inter-observer ICC of < 0.90 were excluded, so the number of GTV, PTV3, PTV6 and PTV9 radiomics

Table 1 Baseline characteristics of lung cancer patients

Characteristics	Training cohort ($n=591$)			Validation cohort ($n=253$)			p value[#]
	pN + group ($n=129$)	pN- group ($n=462$)	p value	pN + group ($n=55$)	pN- group ($n=198$)	p value	
Age[†] (years)	59.0 (52.0, 64.0)	60.0 (53.0, 65.0)	0.079	59.0 (51.0, 63.0)	60.0 (54.0, 64.0)	0.218	0.658
Sex			0.504			0.395	0.470
Male	66 (51.2)	221 (47.8)		28 (50.9)	88 (44.4)		
Female	63 (48.8)	241 (52.2)		27 (49.1)	110 (55.6)		
Smoking history			0.642			0.680	0.424
Never	54 (41.9)	204 (44.2)		27 (49.1)	91 (46.0)		
Current/former	75 (58.1)	258 (55.8)		28 (50.9)	107 (54.0)		
CEA (μg/L)			< 0.001**			0.020*	0.653
Normal (≤ 5)	78 (60.5)	369 (79.9)		36 (65.5)	159 (80.3)		
Abnormal (>5)	51 (39.5)	93 (20.1)		19 (34.5)	39 (19.7)		
TPSA (U/L)			0.865			0.540	0.649
Normal (≤ 80)	97 (75.2)	344 (74.5)		42 (76.4)	143 (72.2)		
Abnormal (>80)	32 (24.8)	118 (25.5)		13 (23.6)	55 (27.8)		
SCC (ug/L)			0.258			0.527	0.258
Normal (≤ 1.5)	117 (90.7)	402 (87.0)		51 (92.7)	178 (89.9)		
Abnormal (> 1.5)	12 (9.3)	60 (13.0)		4 (7.3)	20 (10.1)		
ProGRP (ng/L)			0.120			0.391	0.816
Normal (≤ 63)	127 (98.4)	441 (95.5)		52 (94.5)	192 (97.0)		
Abnormal (>63)	2 (1.6)	21 (4.5)		3 (5.5)	6 (3.0)		
NSE (μg/L)			0.307			0.533	0.570
Normal (≤ 16.3)	119 (92.2)	412 (89.2)		50 (90.9)	174 (87.9)		
Abnormal (> 16.3)	10 (7.8)	50 (10.8)		5 (9.1)	24 (12.1)		
Cyfra21-1 (μg/L)			0.786			0.716	0.995
Normal (≤ 3.3)	90 (69.8)	328 (71.0)		40 (72.7)	139 (73.5)		
Abnormal (> 3.3)	39 (30.2)	134 (29.0)		15 (27.3)	59 (26.5)		
Histologic type			0.190			0.499	0.774
ADC	111 (86.0)	373 (80.7)		46 (83.6)	171 (86.4)		
SCC	9 (7.0)	59 (12.8)		5 (9.1)	23 (11.6)		
Others	9 (7.0)	30 (6.5)		4 (7.3)	4 (2.0)		

CEA, carcinoma embryonic antigen; *TPSA*, tissue polypeptide specific antigen; *SCC*, squamous cell carcinoma antigen; *ProGRP*, pro-gastrin-releasing peptide; *NSE*, neuron specific enolase; *Cyfra 21 – 1*, cytokeratin 19 fragment; *ADC*, adenocarcinoma; *SCC*, squamous cell carcinoma. Except where indicated, data are numbers of patients, with percentages in parentheses

[†] Data are medians, with IQRs in parentheses

[#] Comparison between training cohort and validation cohort

* p value < 0.05, ** p value < 0.001

features was reduced to 1378, 1034, 806 and 722, respectively. After that, independent t-tests identified 1155, 735, 579, and 494 features exhibiting significant differences between the pN + and pN- groups for GTV, PTV3, PTV6, and PTV9, respectively. The PCC and mRMR algorithm were used to identify features that were highly correlated with efficacy but minimally related to other features, and the features of the top 20 were retained. A total of 9, 10, 8, and 9 most predictive radiomic features with nonzero coefficients in the LASSO algorithm were finally selected for Rad-GTV, Rad-PTV3, Rad-PTV6 and Rad-PTV9 (Supplementary Fig. 1). The computed ROC-AUC values for each fold exhibited high consistency (Supplementary Table 3). The SHAP bar chart (Fig. 4) depicted the contribution of the selected features to each radiomics signature. Each Radscore calculation formula was shown in Supplementary Text 2.

Rad-GTV, Rad-PTV3, Rad-PTV6 and Rad-PTV9 were significantly higher in the pN + group compared with pN- group (all $p < 0.001$) (Supplementary Fig. 2). The AUC value of PTV radiomics model increased with the tumor's peripheral expansion distance went further away from the tumor (Table 3). The radiomics signature of PTV9 displayed better performance than the other two PTV radiomics models, and the AUC reached 0.761 (95% CI: 0.716–0.806) and 0.733 (95% CI: 0.663–0.804) in the training and validation cohorts, respectively. Consequently, the PTV9 radiomics signature was selected for further construction of the GPTV model. Based on the respective Rad-score of GTV and PTV9, GPTV model was constructed using binary logistic regression analysis

Table 2 CT imaging features of the entire cohorts in lung cancer patients

CT imaging features	Training cohort ($n=591$)			Validation cohort ($n=253$)		
	pN + group ($n=129$)	pN- group ($n=462$)	*p* value	pN + group ($n=55$)	pN- group ($n=198$)	*p* value
MAD† (mm)	33.0 (25.8, 39.8)	24.7 (17.9, 35.0)	< 0.001**	31.1 (25.6, 41.2)	23.6(16.0, 36.1)	< 0.001**
SAD† (mm)	25.2 (18.6, 33.9)	18.8 (13.5, 26.1)	< 0.001**	25.2 (20.0, 31.8)	18.1 (11.9, 26.9)	< 0.001**
Mean diameter† (mm)	29.5 (21.9, 36.4)	21.5 (16.0, 30.0)	< 0.001**	28.4 (22.5, 36.2)	20.8 (14.3, 31.9)	< 0.001**
Tumor affiliated lobe			0.411			0.552
Right upper lobe	42 (32.6)	147 (31.8)		22 (40.0)	76 (38.4)	
Right middle lobe	5 (3.9)	42 (9.1)		1 (1.8)	11 (5.6)	
Right lower lobe	28 (21.7)	87 (18.8)		13 (23.6)	36 (18.2)	
Left upper lobe	34 (26.3)	116 (25.1)		14 (25.5)	46 (23.2)	
Left lower lobe	20 (15.5)	70 (15.2)		5 (9.1)	29 (14.6)	
Spiculation			0.134			0.507
Absence	45 (34.9)	195 (42.2)		25 (45.5)	100 (50.5)	
Presence	84 (65.1)	267 (57.8)		30 (54.5)	98 (49.5)	
Lobulation			< 0.001**			0.001*
Absence	12 (8.5)	109 (25.5)		4 (10.7)	60 (22.7)	
Presence	117 (91.5)	353 (74.5)		51 (89.3)	138 (77.3)	
Air bronchogram			0.364			0.073
Absence	92 (72.3)	310 (67.4)		46 (76.8)	142 (72.5)	
Presence	37 (27.7)	152 (32.6)		9 (23.2)	56 (27.5)	
Vacuole sign			0.168			0.166
Absence	90 (66.9)	292 (64.9)		32 (75.0)	135 (65.2)	
Presence	39 (33.1)	170 (35.1)		23 (25.0)	63 (34.8)	
Vascular convergence			0.232			0.207
Absence	117 (92.3)	433 (94.2)		54 (91.1)	186 (94.2)	
Presence	12 (7.7)	29 (5.8)		1 (8.9)	12 (5.8)	
Tumor–pleura relationship			< 0.001**			< 0.001**
Type I	27 (20.9)	197 (42.6)		8 (14.5)	86 (43.4)	
Type II	102 (79.1)	265 (57.4)		47 (85.5)	112 (56.6)	

MAD, maximum axial diameter; *SAD*, short axial diameter

Except where indicated, data are numbers of patients, with percentages in parentheses

† Data are medians, with IQRs in parentheses

* *p* value < 0.05, ** *p* value < 0.001

(Supplementary Text 3). The waterfall plot, which ranked patients' scores from smallest to largest, showed patients with a GPTV Rad-score higher than the cutoff value (0.362) was mostly pN+ (Fig. 5). The AUC of Rad-GPTV increased to 0.799 (95% CI: 0.760–0.838) in the training cohort and 0.772 (95% CI: 0.710–0.833) in the validation cohort, and compared with Rad-GTV, Rad-PTV3, Rad-PTV6, and Rad-PTV9, the diagnostic efficiency has improved to some extent (Fig. 6, Supplementary Table 4).

Subgroup analysis based on histological type

We conducted subgroup analysis to compare the diagnostic performance of different PTV and GPTV radiomics models based on histological type (Supplementary Table 5). In the adenocarcinoma group, the AUCs of the radiomics models exhibited a progressive increase in conjunction with the expansion distance of GTV. Notably, the Rad-PTV9 exhibited the most favorable diagnostic performance, with an AUC of 0.784 (95% CI: 0.745–0.823); whereas in the squamous cell carcinoma group, Rad-PTV6 achieved the highest AUC of 0.693 (95% CI: 0.532–0.853) compared to Rad-PTV3 and Rad-PTV9. However, the disparities observed between different PTV models did not reach statistical significance (all $p > 0.05$). Additionally, we constructed GPTV radiomics models by combining GTV with PTV3, PTV6, and PTV9 through binary logistic regression, respectively. The GPTV9 radiomics model and GPTV6 radiomics model exhibited relatively higher predictive performance in the adenocarcinoma group and squamous cell carcinoma group, with AUC of 0.825 (95% CI: 0.792–0.858) and 0.691 (95% CI: 0.528–0.853), respectively.

Development of the clinical-radiomics nomogram and its clinical utility evaluation

A clinical-radiomics model that combined the CEA level, lobulation sign, tumor–pleura relationship, and Rad-GPTV was constructed (Supplementary Text 4)

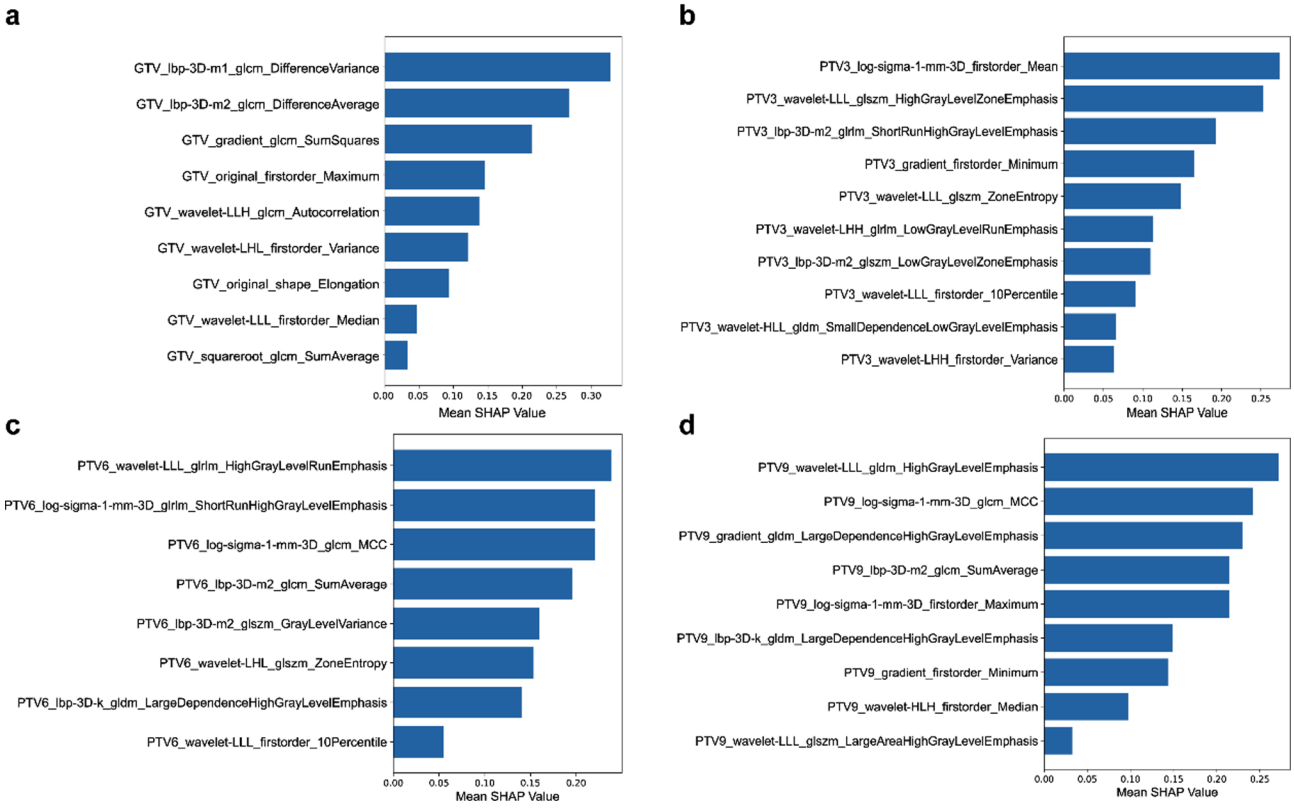

Fig. 4 SHAP bar chart displaying the weights of features in the (**a**) GTV model, (**b**) PTV3 model, (**c**) PTV6 model, (**d**) PTV9 model

Table 3 The prediction model performance in training and validation cohorts

Model	Group	AUC	Sensitivity (%)	Specificity (%)	Accuracy (%)
Clinical model	Training cohort	0.676 (0.628–0.724)	81.4 (73.6–87.7)	45.5 (40.8–50.1)	53.3 (49.2–57.4)
	Validation cohort	0.706 (0.637–0.775)	81.8 (69.1–90.9)	50.0 (42.8–57.2)	56.9 (50.6–63.1)
Radiomics models					
Rad-GTV	Training cohort	0.770 (0.729–0.811)	72.1 (63.5–79.6)	72.3 (68.0-76.3)	72.3 (68.5–75.8)
	Validation cohort	0.749 (0.684–0.814)	61.8 (47.7–74.6)	72.7 (66.0-78.8)	70.4 (64.3–75.9)
Rad-PTV3	Training cohort	0.729 (0.683–0.774)	65.1 (56.2–73.3)	71.2 (66.8–75.3)	69.9 (66.0-73.6)
	Validation cohort	0.702 (0.630–0.774)	54.6 (40.6–68.0)	70.2 (63.3–76.5)	66.8 (60.6–72.6)
Rad-PTV6	Training cohort	0.738 (0.692–0.784)	83.0 (75.3–89.0)	55.2 (50.5–59.8)	61.3 (57.2–65.2)
	Validation cohort	0.709 (0.638–0.780)	76.4 (63.0-86.8)	54.6 (47.3–61.6)	59.3 (53.0-65.4)
Rad-PTV9	Training cohort	0.761 (0.716–0.806)	73.6 (65.2–81.0)	68.0 (63.5–72.2)	69.2 (65.3–72.9)
	Validation cohort	0.733 (0.663–0.804)	58.2 (44.1–71.3)	71.7 (64.9–77.9)	68.8 (62.7–74.4)
Rad-GPTV	Training cohort	0.799 (0.760–0.838)	68.2 (59.4–76.1)	79.0 (75.0-82.6)	76.7 (73.0–80.0)
	Validation cohort	0.772 (0.710–0.833)	56.4 (42.3–69.7)	80.8 (74.6–86.0)	75.5 (69.7–80.7)
Clinical-radiomics model	Training cohort	0.819 (0.780–0.857)	86.1 (78.8–91.5)	63.9 (59.3–68.2)	68.7 (64.8–72.4)
	Validation cohort	0.801 (0.741–0.860)	81.8 (69.1–90.9)	69.2 (62.3–75.5)	71.9 (66.0-71.4)

Values in parentheses represent the 95% confidence interval (CI)

and presented as a predictive nomogram (Fig. 7). The clinical-radiomics model displayed better performance than clinical model ($p < 0.001$; $p = 0.011$) and GPTV model ($p = 0.043$; $p = 0.206$), with an AUC of 0.819 (95% CI: 0.780–0.857) in the training cohort and 0.801 (95% CI: 0.741–0.860) in the validation cohort (Fig. 8). Using the optimal cutoff value, the sensitivity, specificity, and accuracy for the training cohort were 86.1%, 63.9%, and 68.7%, whereas those for the validation cohort were 81.8%, 69.2% and 71.9%, respectively (Table 3).

The calibration curves of the clinical-radiomics model indicated good agreement between predicted and pathological LN metastasis in both cohorts, and Hosmer–Lemeshow goodness-of-fit test revealed no significant differences between the expected and observed values (Fig. 9). Compared with scenarios in which no prediction

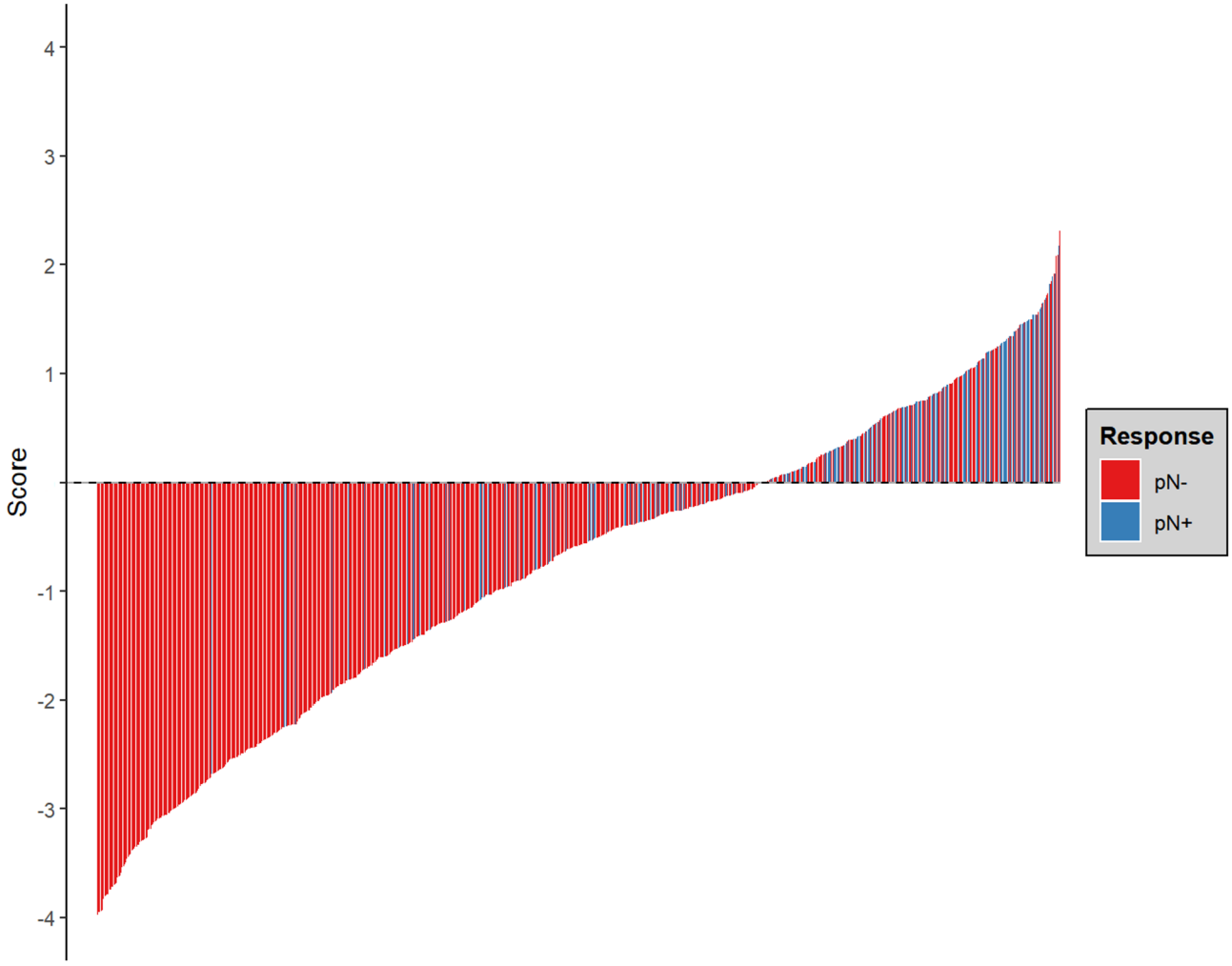

Fig. 5 Waterfall plot for GPTV Rad-score in the whole cohort

model was used (i.e., treat-all or treat-none scheme), the clinical-radiomics model provided a better net benefit for predicting OLNM than the clinical model and GPTV radiomics model at most risk thresholds (Fig. 10). Two illustrative cases diagnosed using the clinical-radiomics nomogram were shown in Fig. 11.

Discussion

Through this study, we developed a machine learning model for prediction of OLNM in patients with peripheral lung cancer by combining clinical data with imaging profiles of sematic features and radiomics features extracted from primary tumor and peritumoral region. The clinical-radiomics model demonstrated superior performance to conventional clinical model and single-modality radiomics prediction models. Our study provided an easy-to-use tool that can be incorporated into routine clinical practice to predict OLNM noninvasively, which could enable clinicians to design more effective therapeutic regimens.

Previous studies have identified clinical biomarkers to predict LN metastasis in lung cancer patients. In the present study, patients with elevated CEA level above the upper limits tended to be more likely to have OLNM, which was in line with previous findings [22, 23]. Significant differences were observed in the expression of serum CEA, NSE, Cyfra 21 – 1, SCC-Ag and ProGRP among lung cancer patients with different pathological types, and compared with other serum tumor markers, CEA showed the highest expression in lung adenocarcinoma [33]. In our study, 83.06% of the patients were diagnosed with lung adenocarcinoma (701/844), which was presumed to account for the variation in CEA levels among numerous lung tumor markers between pN + and pN- groups.

Conventional CT interpretation, namely semantic features can provide morphological, internal, and peripheral features of lung tumors. There is currently no consistent conclusion on whether semantic features of primary lung tumor are helpful in predicting LN metastasis and which

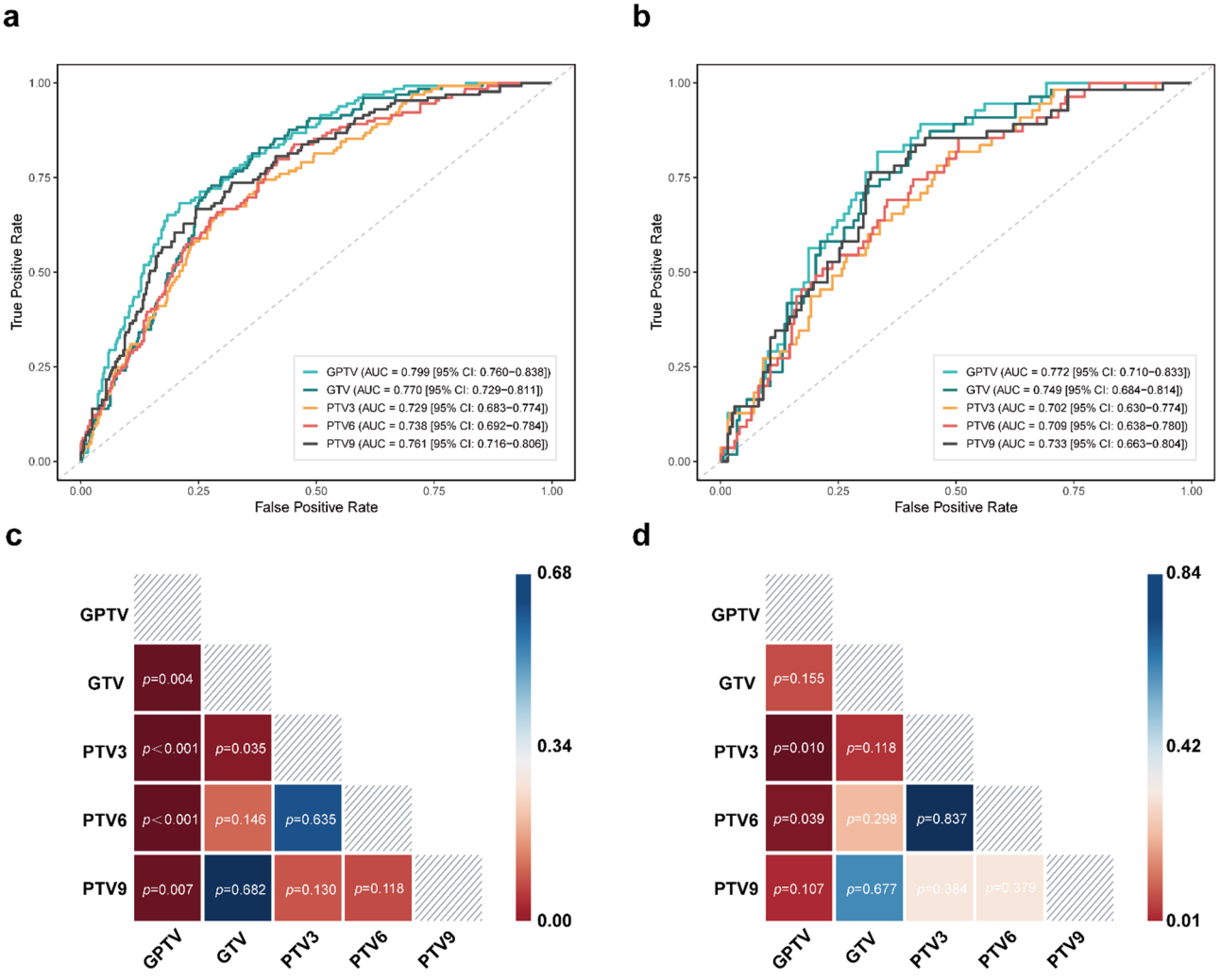

Fig. 6 Receiver operating characteristic (ROC) curves of different radiomics signature and heatmaps showing pairwise area under the curve (AUC) comparisons using Delong's test in the training (**a**, **c**) and validation (**b**, **d**) cohorts

features are highly risk factors for OLNM. Several studies have confirmed that visceral pleural invasion was closely related to LN metastasis [28, 34–37]. Consistent with these studies, we observed a higher prevalence of type II tumor-pleura relationship in pN + group. Multivariable logistic regression analysis showed that CEA level, lobulation sign and tumor–pleura relationship were independent predictors for OLNM. However, this clinical model could not provide satisfactory diagnostic performance, since the diagnostic specificity and accuracy are relatively low, only around 50%.

Radiomics features (such as first-order statistics, shape, and textural features) are associated with tumor biological behaviors, including gene expression patterns, lymph node metastasis, tumor immune microenvironment, and prognosis [38–40]. Although a few studies have proven the feasibility of radiomics analysis of primary tumor and peritumoral region to predict LN metastasis [18, 20, 22, 23, 26, 41–43], there exists inconsistency in the extent of tumor expansion beyond the primary site, leading to certain discrepancies in their conclusions. Histopathological examination of micrometastatic patterns in NSCLC specimens identified significant quantitative morphological differences between adenocarcinoma and squamous cell carcinoma. Microscopic extension (ME) measurements demonstrated significantly greater mean values in adenocarcinoma (2.69 mm) compared to squamous cell carcinoma (1.48 mm), with statistical significance ($p = 0.01$). To achieve 95% probability of encompassing microscopic disease extension, the proposed safety margins (defined as optimal peripheral tissue coverage thresholds) were calculated as 8 mm for adenocarcinoma and 6 mm for squamous cell carcinoma [44]. Additionally, Grills et al. [45] observed that the mean microscopic extension distance for lung adenocarcinoma exhibited a significant inverse correlation with histological grade ($p < 0.01$). For a GTV contoured on the CT lung windows, the margin required to cover microscopic extension for 90% of the

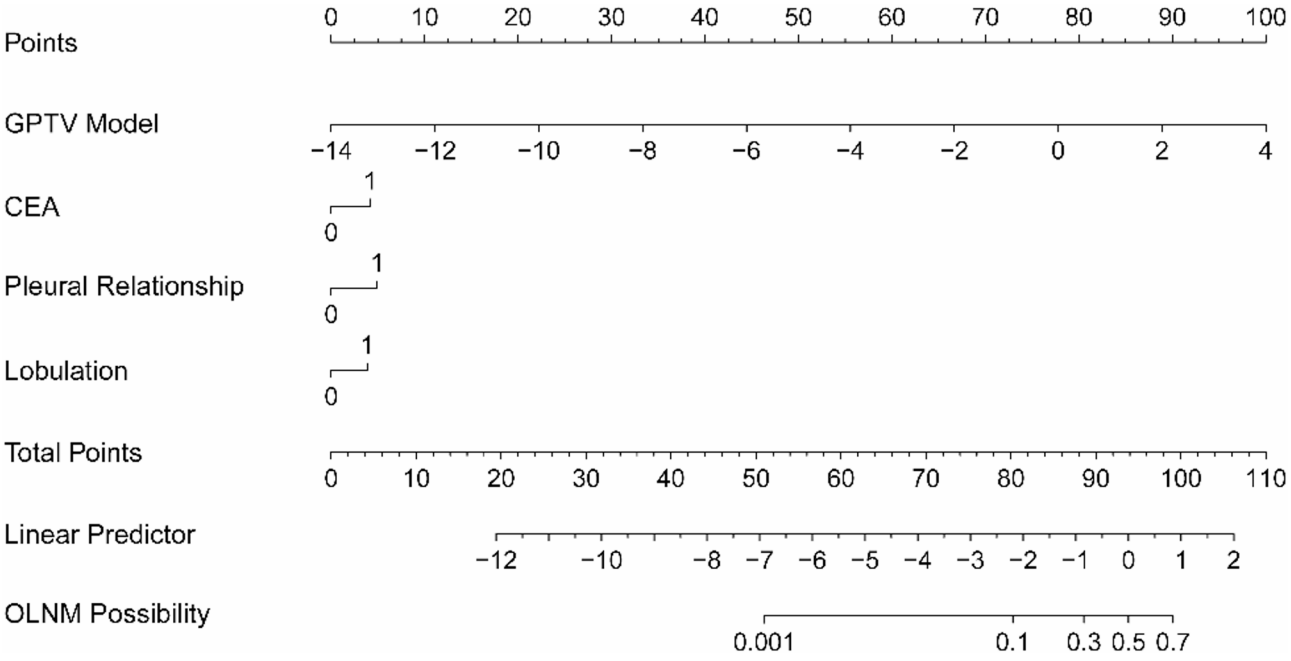

Fig. 7 The clinical-radiomics nomogram that integrates CEA level, tumor–pleura relationship, lobulation sign, and Rad-GPTV for predicting occult lymph node metastasis (OLNM)

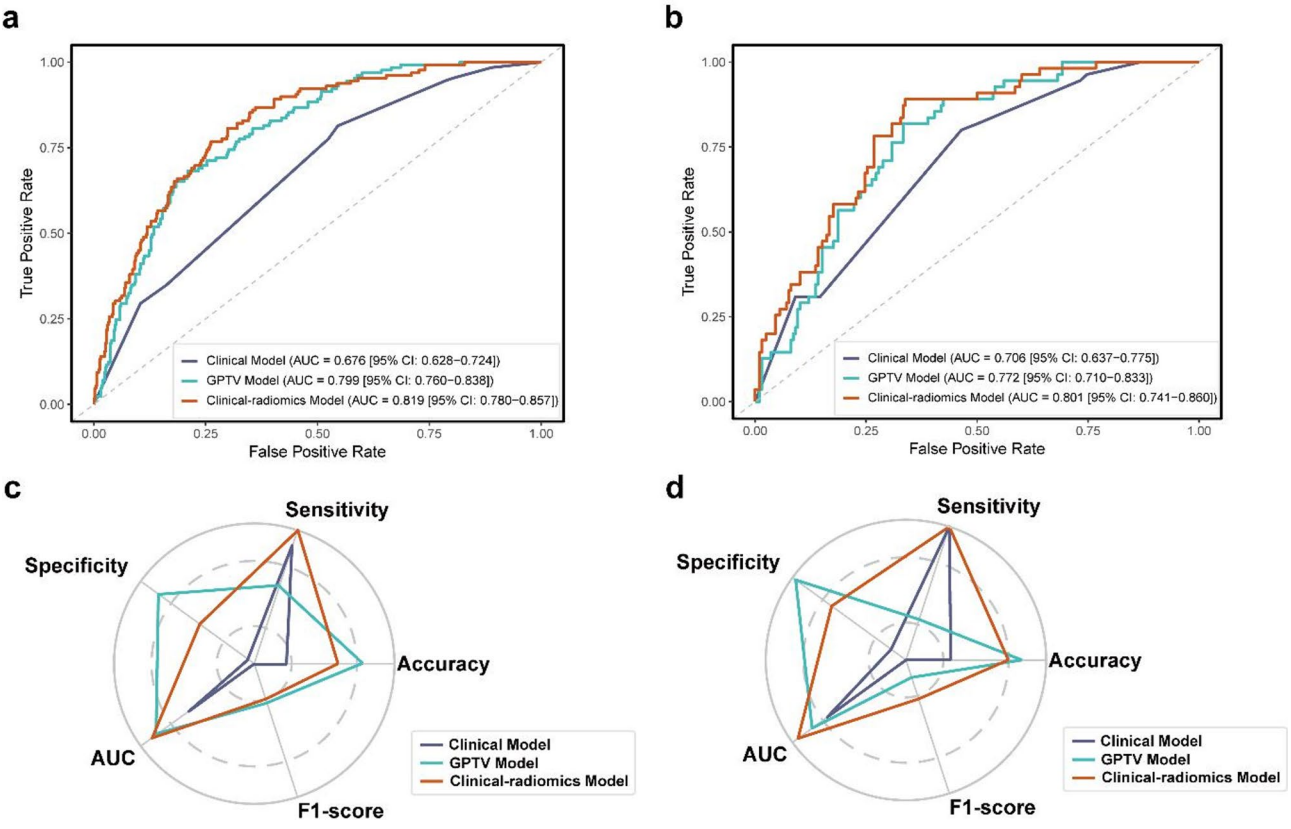

Fig. 8 Receiver operating characteristic (ROC) curves and radar chat for clinical model, GPTV radiomics model and clinical-radiomics model in the (**a, c**) training and (**b, d**) validation cohorts

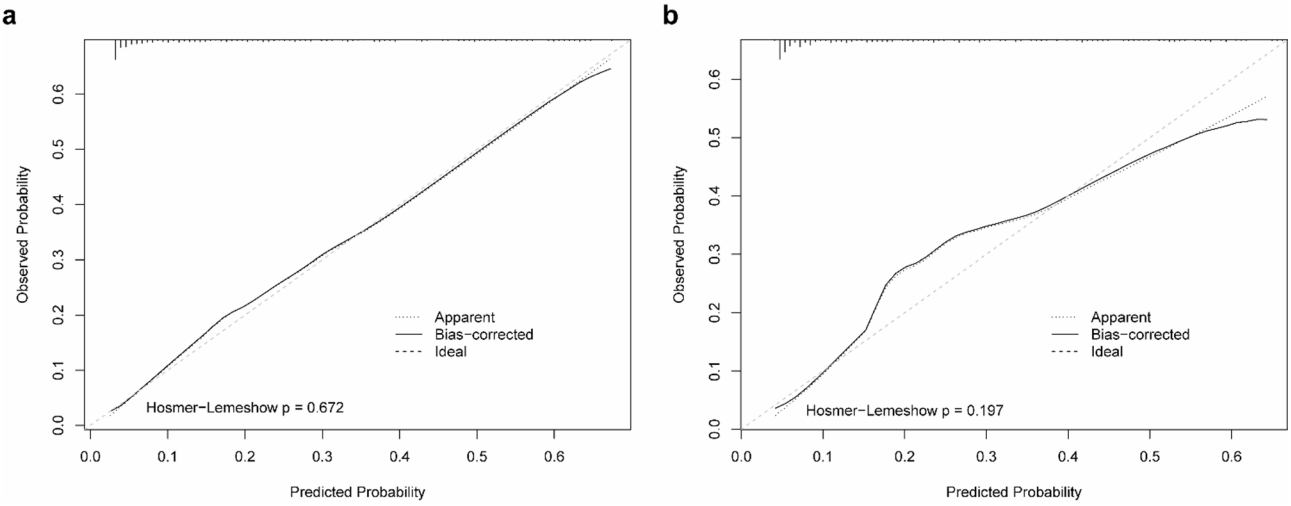

Fig. 9 Calibration curve of clinical-radiomics prediction model in the training cohort (**a**) and validation cohort (**b**). The actual occult lymph node metastasis (OLNM) rate was represented on the Y-axis and the predicted OLNM probability was represented on the X-axis

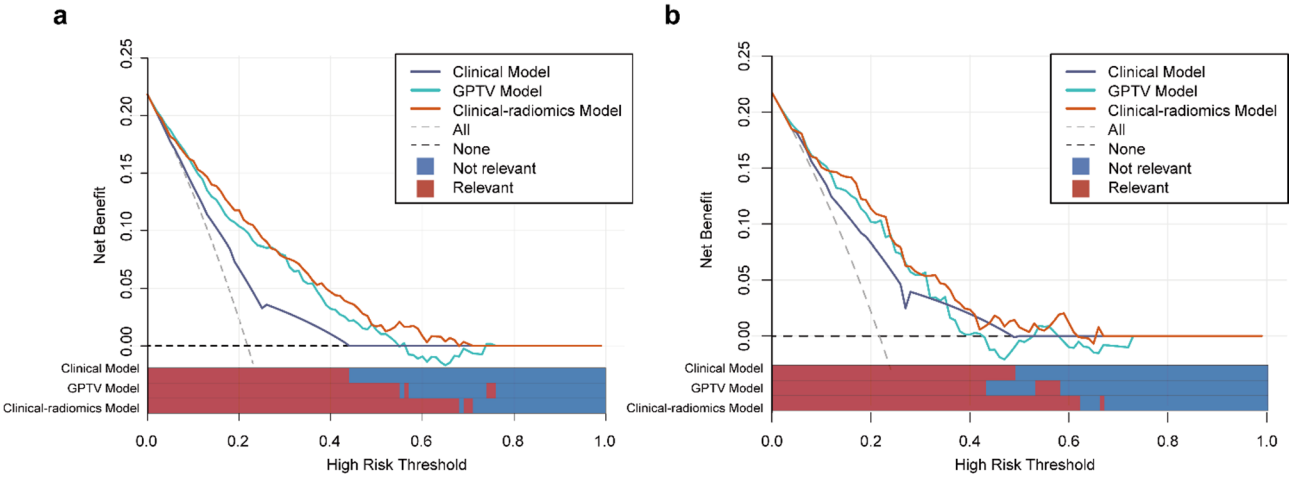

Fig. 10 Decision curve analysis (DCA) of each model in the training cohort (**a**) and validation cohort (**b**). The Y-axis represents net benefit. The X-axis represents threshold probability. The clinical-radiomics model added more benefit to predict OLNM than the clinical model, GPTV model, and the "treating all or none" scheme at most risk thresholds. The bar graph presented beneath the DCA plot depicts the distribution of net benefit across various models

cases would be 9 mm (9, 7, and 4 mm for Grade 1 to 3, respectively). Furthermore, the peritumoral microenvironment within a 3 to 9 mm radius of lung adenocarcinoma has been shown to harbor biological information that is closely linked to tumor heterogeneity [46]. Therefore, instead of using an arbitrarily defined peritumoral region, we established three different peripheral extension distances of 3 mm, 6 mm, and 9 mm. The results showed that the radiomics signature of PTV9 showed equivalent diagnostic performance to GTV model, but improved predictability compared to PTV3 and PTV6 models. In addition, we performed subgroup analyses based on histologic type. The results revealed that the PTV6-based radiomics model achieved the highest diagnostic efficacy in patients with squamous cell carcinoma, while the PTV9-based model performed best in those with adenocarcinoma. These findings are consistent with previous pathological studies showing that adenocarcinoma typically exhibits greater microscopic extension than squamous cell carcinoma [44]. Notably, in our study population, adenocarcinoma constituted the majority of cases, followed by squamous cell carcinoma. Although the PTV6 model showed relatively higher AUC in the squamous cell carcinoma group, the differences among the models did not reach statistical significance. Thus, PTV9 was chosen as the optimal tumor extension distance for PTV modeling.

Given that primary tumors accumulating more heterogeneous subclones tend to disseminate and aggressive malignant tumors have the capacity to infiltrate neighboring tissues [47], GPTV model was established by integrating Rad-score of GTV and PTV9, which was different

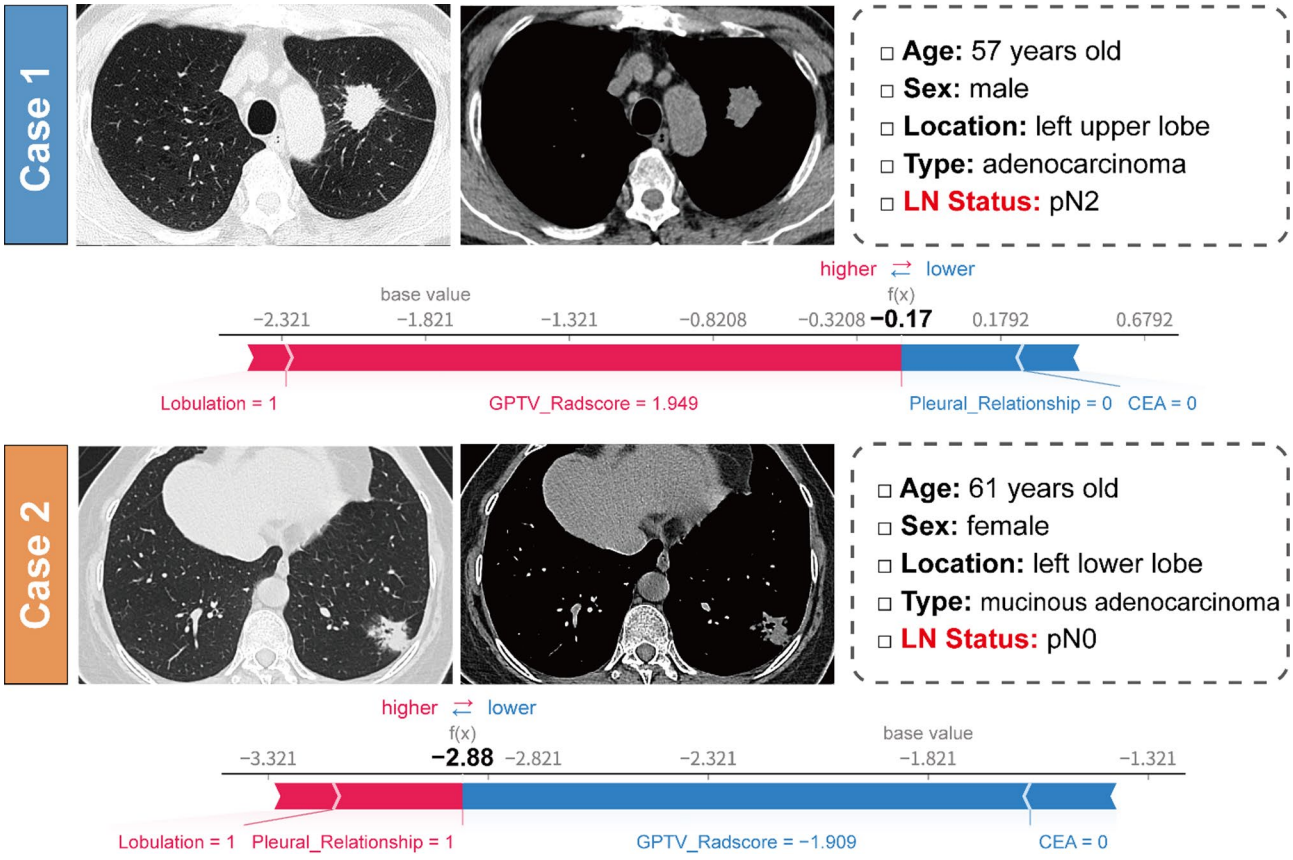

Fig. 11 Individual visualization of the mode through SHAP. **Case 1**: A 57-year-old man with invasive lung adenocarcinoma in the left upper lobe (pN2). The longest tumor diameter was 32.6 mm. The tumor manifested as an irregular mass with lobulation and spiculation, and had linear shadows between tumor and pleura on lung window images but was not observed on mediastinal window images (Type I). The SHAP force plot illustrates the contribution of each feature to the model's predicted probability of occult lymph node metastasis (OLNM). Key factors including lobulation = "1", pleural relationship = "0", and a high GPTV_Radscore (1.949) strongly pushed the prediction toward a higher risk, whereas CEA = "0" had a minimal pulling effect toward lower risk. The final SHAP output value was 0.55, indicating a relatively high predicted probability of OLNM. Based on the clinical-radiomics nomogram, this case demonstrated an 83.90% probability of OLNM. **Case 2**: A 61-year-old woman with invasive mucinous adenocarcinoma in the left lower lobe (pN0). The tumor measured 28.2 mm in its longest diameter and appeared as an irregular mass with lobulated margins. The tumor adhered to the pleura characterized by a broad base, classified as Type II. The SHAP force plot shows that although lobulation = "1" and pleural relationship = "1" contributed positively toward higher risk, a markedly low GPTV_Radscore (−1.909) exerted a dominant negative contribution, pulling the prediction toward lower risk. The final SHAP value was − 2.87, corresponding to a lower predicted probability of OLNM. Based on the clinical-radiomics nomogram, this case showed a 13.55% probability of OLNM

from the strategy of considering the entire tumor and peritumoral volume as a whole VOI to construct GPTV model [26]. This discrepancy may be attributed to the fact that the tumor size was not restricted to a certain clinical stage in the current study, if the same outward expansion distance was delineated, the proportion of tumor components in the GPTV as a whole VOI would be significantly different among tumors of different sizes, which may cause significant changes in certain radiomics features between GTV and GPTV.

Our analysis demonstrated that the GPTV radiomics model achieved superior discriminative capacity among comparative radiomic frameworks, as evidenced by its higher AUC values compared to both GTV and PTV models. This observation corroborates prior research establishing the prognostic value of intratumoral and peritumoral radiomic signatures for detecting lymphovascular invasion (LVI) in NSCLC, with the GPTV9 configuration showing the best prediction performance [48]. The clinical significance of these findings is reinforced by the evidence that the presence of LVI significantly increases the risk of nodal recurrence [49]. Mechanistic insights derived from the GPTV9 architecture suggest that combining tumor core and peripheral characteristics may enhance detection sensitivity for metastatic nodal involvement, particularly in identifying radiologically OLNM.

By combining the advantages of microscopic radiomic features and macroscopic clinical features, a nomogram which was composed of CEA level, lobulation sign, tumor–pleura relationship and Rad-GPTV demonstrated excellent performance of predicting OLNM in both

training cohort (AUC = 0.819, 95% CI: 0.780–0.857) and validation cohort (AUC = 0.801, 95% CI: 0.741–0.860) with robust accuracy, suggesting that this clinical-radiomics model might be generalizable to real-world scenarios.

Despite the remarkable results, there are still some potential drawbacks associated with our study, which must be taken into account. First, this was a retrospective and single-center study, thus case selection bias was inevitable. A large prospective investigation among multicenter is necessary. Second, the variability of CT scanners and image acquisition protocols may reflect a diverse practice, making the constructed model trained using these data better suited to clinical application in a real-world setting, but it may have an impact on the results. Third, it may be more promising to combine radiomics features of primary lung cancers and LNs; however, it is rather difficult to match the precise locations of surgically resected lymph nodes with their counterparts in CT images. Ultimately, manual segmentation is a time-consuming and labor-intensive task, and some variability during this procedure may affect the prediction performance.

Conclusion

The machine learning model utilizing CT radiomics features extracted from primary lesion and its surrounding lung parenchyma can effectively predict OLNM in peripheral lung cancer patients. The clinical-radiomics model integrating independent clinical predictor, CT semantic features of the tumor, GTV and PTV9 radiomics features (Rad-GPTV) demonstrated the best predictive performance, which can be served as a noninvasive preoperative prediction tool for personalized risk assessment of OLNM in lung cancer patients.

Abbreviations

LN	Lymph node
NSCLC	Non-small cell lung cancer
CT	Computed tomography
OLNM	Occult lymph node metastasis
GGO	Ground-glass opacity
NSE	Neuron specific enolase
CEA	Carcinoma embryonic antigen
TPSA	Tissue polypeptide specific antigen
SCC-Ag	Squamous cell carcinoma antigen
ProGRP	Pro-gastrin-releasing peptide
Cyfra 21 – 1	Cytokeratin 19 fragment
pN+	Pathological lymph node positive
pN-	Pathological lymph node negative
GTV	Gross tumor volume
PTV	Peri-tumoral volume
GLCM	Gray-level co-occurrence matrix
GLDM	Gray-level dependence matrix
GLRLM	Gray-level run length matrix
GLSZM	Gray-level size zone matrix
NGTDM	Neighboring gray tone difference matrix
SMOTE	Synthetic minority oversampling technique
ICC	Intraclass Correlation Coefficient
PCC	Pearson Correlation Coefficient
mRMR	Minimum redundancy maximum relevance
LASSO	The least absolute shrinkage and selection operator (LASSO)
LR	Logistic Regression
ROC	Receiver operating characteristics
SHAP	SHapley Addictive exPlanations
DCA	Decision curve analysis
OR	Odds ratio
CI	Confidence interval
ME	Microscopic extension
LVI	Lymphovascular invasion

Supplementary Information

The online version contains supplementary material available at https://doi.org/10.1186/s40644-025-00928-3.

Supplementary Material 1

Supplementary Material 2

Acknowledgements

Not applicable.

Author contributions

Conceptualization and design: YL and XL; Data curation and assembly of data: XL, FL, JE, XC and XW; Formal analysis: XL, FL, JY and YZ; Writing – review & editing: all authors; Supervision: BS and YL; Final approval of manuscript: all authors.

Funding

This study was supported by the National Natural Science Foundation of China (Grant No. 82472063), The Chinese National Key Research and Development Project (Grant No. 2021YFC2500400 and Grant No.2021YFC2500402), and Tianjin Key Medical Specialist Construction Project (No. TJYXZDXK-010 A).

Data availability

No datasets were generated or analysed during the current study.

Declarations

Ethics approval and consent to participate

This study was conducted in line with the Declaration of Helsinki. The requirement for patient informed consent was waived by our institutional review board due to the retrospective study design.

Consent for publication

Not applicable.

Competing interests

The authors declare no competing interests.

Author details

[1]Department of Radiology, Tianjin Medical University Cancer Institute & Hospital, National Clinical Research Center for Cancer; Tianjin's Clinical Research Center for Cancer; Key Laboratory of Cancer Immunology and Biotherapy, Tianjin, Huan-Hu-Xi Road, Ti-Yuan-Bei, He Xi District, Tianjin, China

[2]Department of Lung Cancer, Tianjin Medical University Cancer Institute & Hospital, National Clinical Research Center for Cancer; Tianjin's Clinical Research Center for Cancer; Key Laboratory of Cancer Prevention and Therapy, Tianjin; , Huan-Hu-Xi Road, Ti-Yuan-Bei, He Xi District, Tianjin, China

Received: 1 June 2025 / Accepted: 12 August 2025
Published online: 21 August 2025

References

1. Sung H, Ferlay J, Siegel RL, Laversanne M, Soerjomataram I, Jemal A, Bray F. Global cancer statistics 2020: GLOBOCAN estimates of incidence and mortality worldwide for 36 cancers in 185 countries. CA Cancer J Clin. 2021;71(3):209–49.
2. Rami-Porta R, Nishimura KK, Giroux DJ, Detterbeck F, Cardillo G, Edwards JG, Fong KM, Giuliani M, Huang J, Kernstine KH, editors. Sr. : The International Association for the Study of Lung Cancer Lung Cancer Staging Project: Proposals for Revision of the TNM Stage Groups in the Forthcoming (Ninth) Edition of the TNM Classification for Lung Cancer. J Thorac Oncol. 2024;19(7):1007–1027.
3. Chan EG, Chan PG, Mazur SN, Normolle DP, Luketich JD, Landreneau RJ, Schuchert MJ. Outcomes with segmentectomy versus lobectomy in patients with clinical T1cN0M0 non-small cell lung cancer. J Thorac Cardiovasc Surg. 2021;161(5):1639–e16481632.
4. Roman M, Labbouz S, Valtzoglou V, Ciesla A, Hawari M, Addae-Boateng E, Thorpe JA, Duffy JP, Majewski A. Lobectomy vs. Segmentectomy. A propensity score matched comparison of outcomes. Eur J Surg Oncol. 2019;45(5):845–50.
5. Al-Thani S, Nasar A, Villena-Vargas J, Harrison S, Lee B, Port JL, Altorki N, Chow OS. Wedge resection, segmentectomy, and lobectomy: oncologic outcomes based on extent of surgical resection for =2 cm stage IA non-small cell lung cancer</at. J Thorac Dis. 2024;16(3):1875–84.
6. Ichinose J, Yamamoto H, Aokage K, Kondo H, Sato Y, Suzuki K, Chida M. Real-world perioperative outcomes of segmentectomy versus lobectomy for early-stage lung cancer: a propensity score-matched analysis. Eur J Cardiothorac Surg 2022, 63(1).
7. Kamigaichi A, Mimae T, Amioka J, Aoki G, Yoshimura K, Kawamoto N, Tsubokawa N, Miyata Y, Okada M. Segmentectomy preserves better immune-nutritional status than lobectomy in patients with early-stage lung cancer. Eur J Cardiothorac Surg 2023, 63(2).
8. Deng H, Zhou J, Chen H, Cai X, Zhong R, Li F, Cheng B, Li C, Jia Q, Zhou C, et al. Impact of lymphadenectomy extent on immunotherapy efficacy in postresectional recurred non-small cell lung cancer: a multi-institutional retrospective cohort study. Int J Surg. 2024;110(1):238–52.
9. Webb WR, Gatsonis C, Zerhouni EA, Heelan RT, Glazer GM, Francis IR, McNeil BJ. CT and MR imaging in staging non-small cell bronchogenic carcinoma: report of the radiologic diagnostic oncology group. Radiology. 1991;178(3):705–13.
10. Wang B, Sun K, Meng X, Bhuva MS, Sun X, Sun Y. The different evaluative significance of enlarged lymph nodes on preoperative CT in the N stage for patients with suspected subsolid and solid lung cancers. Acad Radiol. 2023;30(7):1392–9.
11. Park HK, Jeon K, Koh WJ, Suh GY, Kim H, Kwon OJ, Chung MP, Lee KS, Shim YM, Han J, et al. Occult nodal metastasis in patients with non-small cell lung cancer at clinical stage IA by PET/CT. Respirology. 2010;15(8):1179–84.
12. Beyaz F, Verhoeven RLJ, Schuurbiers OCJ, Verhagen A, van der Heijden E. Occult lymph node metastases in clinical N0/N1 NSCLC; A single center in-depth analysis. Lung Cancer. 2020;150:186–94.
13. Qiao J, Zhang X, Du M, Wang P, Xin J. (18)F-FDG PET/CT radiomics nomogram for predicting occult lymph node metastasis of non-small cell lung cancer. Front Oncol. 2022;12:974934.
14. Lambin P, Rios-Velazquez E, Leijenaar R, Carvalho S, van Stiphout RG, Granton P, Zegers CM, Gillies R, Boellard R, Dekker A, et al. Radiomics: extracting more information from medical images using advanced feature analysis. Eur J Cancer. 2012;48(4):441–6.
15. Gillies RJ, Kinahan PE, Hricak H. Radiomics: images are more than pictures, they are data. Radiology. 2016;278(2):563–77.
16. Lu H, Arshad M, Thornton A, Avesani G, Cunnea P, Curry E, Kanavati F, Liang J, Nixon K, Williams ST, et al. A mathematical-descriptor of tumor-mesoscopic-structure from computed-tomography images annotates prognostic- and molecular-phenotypes of epithelial ovarian cancer. Nat Commun. 2019;10(1):764.
17. Zhong Y, Yuan M, Zhang T, Zhang YD, Li H, Yu TF. Radiomics approach to prediction of occult mediastinal lymph node metastasis of lung adenocarcinoma. AJR Am J Roentgenol. 2018;211(1):109–13.
18. Yang X, Pan X, Liu H, Gao D, He J, Liang W, Guan Y. A new approach to predict lymph node metastasis in solid lung adenocarcinoma: a radiomics nomogram. J Thorac Dis. 2018;10(Suppl 7):S807–19.
19. He L, Huang Y, Yan L, Zheng J, Liang C, Liu Z. Radiomics-based predictive risk score: A scoring system for preoperatively predicting risk of lymph node metastasis in patients with resectable non-small cell lung cancer. Chin J Cancer Res. 2019;31(4):641–52.
20. Cong M, Yao H, Liu H, Huang L, Shi G. Development and evaluation of a venous computed tomography radiomics model to predict lymph node metastasis from non-small cell lung cancer. Med (Baltim). 2020;99(18):e20074.
21. Botta F, Raimondi S, Rinaldi L, Bellerba F, Corso F, Bagnardi V, Origgi D, Minelli R, Pitoni G, Petrella F et al. Association of a CT-Based clinical and radiomics score of Non-Small cell lung cancer (NSCLC) with lymph node status and overall survival. Cancers (Basel) 2020, 12(6).
22. Zhang R, Zhang R, Luan T, Liu B, Zhang Y, Xu Y, Sun X, Xing L. A radiomics nomogram for preoperative prediction of clinical occult lymph node metastasis in cT1-2N0M0 solid lung adenocarcinoma. Cancer Manag Res. 2021;13:8157–67.
23. Wang X, Zhao X, Li Q, Xia W, Peng Z, Zhang R, Li Q, Jian J, Wang W, Tang Y, et al. Can peritumoral radiomics increase the efficiency of the prediction for lymph node metastasis in clinical stage T1 lung adenocarcinoma on CT? Eur Radiol. 2019;29(11):6049–58.
24. Das SK, Fang KW, Xu L, Li B, Zhang X, Yang HF. Integrative nomogram of intratumoral, peritumoral, and lymph node radiomic features for prediction of lymph node metastasis in cT1N0M0 lung adenocarcinomas. Sci Rep. 2021;11(1):10829.
25. Li Z, Jiang Y, Liu J, Fu H, Yang Q, Song W, Li Y. Exosomes from PYCR1 knockdown bone marrow mesenchymal stem inhibits aerobic Glycolysis and the growth of bladder cancer cells via regulation of the EGFR/PI3K/AKT pathway. Int J Oncol 2023, 63(1).
26. Chen QL, Li MM, Xue T, Peng H, Shi J, Li YY, Duan SF, Feng F. Radiomics nomogram integrating intratumoural and peritumoural features to predict lymph node metastasis and prognosis in clinical stage IA non-small cell lung cancer: a two-centre study. Clin Radiol. 2023;78(5):e359–67.
27. Lardinois D, De Leyn P, Van Schil P, Porta RR, Waller D, Passlick B, Zielinski M, Lerut T, Weder W. ESTS guidelines for intraoperative lymph node staging in non-small cell lung cancer. Eur J Cardiothorac Surg. 2006;30(5):787–92.
28. Zhang C, Wang L, Cai X, Li M, Sun D, Wang P. Tumour-pleura relationship on CT is a risk factor for occult lymph node metastasis in peripheral clinical stage IA solid adenocarcinoma. Eur Radiol. 2023;33(5):3083–91.
29. Ibrahim A, Refaee T, Primakov S, Barufaldi B, Acciavatti RJ, Granzier RWY, Hustinx R, Mottaghy FM, Woodruff HC, Wildberger JE et al. The Effects of In-Plane Spatial Resolution on CT-Based Radiomic Features' Stability with and without ComBat Harmonization. Cancers. 2021, 13(8).
30. Davey A, van Herk M, Faivre-Finn C, Brown S, McWilliam A. Optimising use of 4D-CT phase information for radiomics analysis in lung cancer patients treated with stereotactic body radiotherapy. Phys Med Biol 2021, 66(11).
31. Song Y, Zhang J, Zhang YD, Hou Y, Yan X, Wang Y, Zhou M, Yao YF, Yang G. FeAture explorer (FAE): A tool for developing and comparing radiomics models. PLoS ONE. 2020;15(8):e0237587.
32. Zwanenburg A, Vallières M, Abdalah MA, Aerts HJWL, Andrearczyk V, Apte A, Ashrafinia S, Bakas S, Beukinga RJ, Boellaard R, et al. The image biomarker standardization initiative: standardized quantitative radiomics for High-Throughput image-based phenotyping. Radiology. 2020;295(2):328–38.
33. Hu J, Zhang L, Xia H, Yan Y, Zhu X, Sun F, Sun L, Li S, Li D, Wang J, et al. Tumor microenvironment remodeling after neoadjuvant immunotherapy in non-small cell lung cancer revealed by single-cell RNA sequencing. Genome Med. 2023;15(1):14.
34. Ding N, Mao Y, Gao S, Xue Q, Wang D, Zhao J, Gao Y, Huang J, Shao K, Feng F, et al. Predictors of lymph node metastasis and possible selective lymph node dissection in clinical stage IA non-small cell lung cancer. J Thorac Dis. 2018;10(7):4061–8.
35. Moon Y, Choi SY, Park JK, Lee KY. Risk factors for occult lymph node metastasis in peripheral Non-Small cell lung cancer with invasive component size 3 cm or less. World J Surg. 2020;44(5):1658–65.
36. Wang Y, Jing L, Wang G. Risk factors for lymph node metastasis and surgical methods in patients with early-stage peripheral lung adenocarcinoma presenting as ground glass opacity. J Cardiothorac Surg. 2020;15(1):121.
37. Chang YL, Lin MW, Shih JY, Wu CT, Lee YC. The significance of visceral pleural surface invasion in 321 cases of non-small cell lung cancers with pleural Retraction. Ann Surg Oncol. 2012;19(9):3057–64.
38. Aerts HJWL, Velazquez ER, Leijenaar RTH, Parmar C, Grossmann P, Carvalho S, Bussink J, Monshouwer R, Haibe-Kains B, Rietveld D, et al. Decoding tumour phenotype by noninvasive imaging using a quantitative radiomics approach. Nat Commun. 2014;5:4006.
39. Wen X, Liu M-W, Qiu B, Wang Y-M, Jiang J-M, Zhang X, Jiang X, Li L, Li M, Zhang L. CT-based radiomic consensus clustering association with tumor

biological behavior in clinical stage IA adenocarcinoma: a retrospective study. Transl Lung Cancer Res. 2024;13(8):1794–806.
40. Bernatowicz K, Amat R, Prior O, Frigola J, Ligero M, Grussu F, Zatse C, Serna G, Nuciforo P, Toledo R et al. Radiomics signature for dynamic monitoring of tumor inflamed microenvironment and immunotherapy response prediction. J Immunother Cancer 2025, 13(1).
41. Fyles TM. Bilayer membranes and transporter models. Curr Opin Chem Biol. 1997;1(4):497–505.
42. Zhu H, Xu Y, Liang N, Sun H, Huang Z, Xie S, Wang W. Assessment of clinical stage IA lung adenocarcinoma with pN1/N2 metastasis using CT quantitative texture analysis. Cancer Manag Res. 2020;12:6421–30.
43. Zheng X, Shao J, Zhou L, Wang L, Ge Y, Wang G, Feng F. A comprehensive nomogram combining CT imaging with clinical features for prediction of lymph node metastasis in stage I-IIIB Non-small cell lung cancer. Ther Innov Regul Sci. 2022;56(1):155–67.
44. Giraud P, Antoine M, Larrouy A, Milleron B, Callard P, De Rycke Y, Carette MF, Rosenwald JC, Cosset JM, Housset M, et al. Evaluation of microscopic tumor extension in non-small-cell lung cancer for three-dimensional conformal radiotherapy planning. Int J Radiat Oncol Biol Phys. 2000;48(4):1015–24.
45. Grills IS, Fitch DL, Goldstein NS, Yan D, Chmielewski GW, Welsh RJ, Kestin LL. Clinicopathologic analysis of microscopic extension in lung adenocarcinoma: defining clinical target volume for radiotherapy. Int J Radiat Oncol Biol Phys. 2007;69(2):334–41.
46. Liu K, Li K, Wu T, Liang M, Zhong Y, Yu X, Li X, Xie C, Zhang L, Liu X. Improving the accuracy of prognosis for clinical stage I solid lung adenocarcinoma by radiomics models covering tumor per se and peritumoral changes on CT. Eur Radiol. 2022;32(2):1065–77.
47. Lue KH, Chu SC, Wang LY, Chen YC, Li MH, Chang BS, Chan SC, Chen YH, Lin CB, Liu SH. Tumor glycolytic heterogeneity improves detection of regional nodal metastasis in patients with lung adenocarcinoma. Ann Nucl Med. 2022;36(3):256–66.
48. Chen Q, Shao J, Xue T, Peng H, Li M, Duan S, Feng F. Intratumoral and peritumoral radiomics nomograms for the preoperative prediction of lymphovascular invasion and overall survival in non-small cell lung cancer. Eur Radiol. 2023;33(2):947–58.
49. Sung SY, Kwak Y-K, Lee S-W, Jo IY, Park JK, Kim KS, Lee KY, Kim Y-S. Lymphovascular invasion increases the risk of nodal and distant recurrence in Node-Negative stage I-IIA Non-Small-Cell lung cancer. Oncology. 2018;95(3):156–62.

Publisher's note